

## Article

# Analysis and Correction of the Crosstalk Effect in a Three-Axis SERF Atomic Magnetometer

Yeguang Yan <sup>1,2</sup>, Jixi Lu <sup>1,2</sup> , Binquan Zhou <sup>1,2,\*</sup>, Kun Wang <sup>1,2</sup>, Ziao Liu <sup>1,2</sup>, Xiaoyu Li <sup>1,2</sup>, Weiyi Wang <sup>1,2</sup> and Gang Liu <sup>1,2</sup>

<sup>1</sup> Key Laboratory of Ultra-Weak Magnetic Field Measurement Technology, Ministry of Education, School of Instrumentation and Optoelectronic Engineering, Beihang University, Beijing 100191, China

<sup>2</sup> Zhejiang Provincial Key Laboratory of Ultra-Weak Magnetic-Field Space and Applied Technology, Hangzhou Innovation Institute, Beihang University, Hangzhou 310051, China

\* Correspondence: bqzhou@buaa.edu.cn

**Abstract:** Three-axis atomic magnetometers have an excellent advantage for determining the complete vector information of a magnetic field to be measured. However, the crosstalk effect, which leads to an error output on one axis owing to a magnetic field on the other axes, can reduce the measurement accuracy. In this study, we propose an effective suppression method for the crosstalk effect in a three-axis atomic magnetometer. First, we investigated and analyzed the main factors that introduce the effect. Based on this, the modulation parameters were optimized to improve the scale factors, which obtained a coupling coefficient of less than 6% for the atomic magnetometer. Subsequently, the associated transfer matrix was corrected to further suppress the crosstalk effect. After correction, all the coupling coefficients were decreased to less than 3%, with the majority being lower than 1%.

**Keywords:** three-axis magnetometer; crosstalk effect; density matrix equation; magnetic fields measurement



**Citation:** Yan, Y.; Lu, J.; Zhou, B.; Wang, K.; Liu, Z.; Li, X.; Wang, W.; Liu, G. Analysis and Correction of the Crosstalk Effect in a Three-Axis SERF Atomic Magnetometer. *Photonics* **2022**, *9*, 654. <https://doi.org/10.3390/photonics9090654>

Received: 30 August 2022

Accepted: 13 September 2022

Published: 14 September 2022

**Publisher's Note:** MDPI stays neutral with regard to jurisdictional claims in published maps and institutional affiliations.



**Copyright:** © 2022 by the authors. Licensee MDPI, Basel, Switzerland. This article is an open access article distributed under the terms and conditions of the Creative Commons Attribution (CC BY) license (<https://creativecommons.org/licenses/by/4.0/>).

## 1. Introduction

Atomic magnetometers have been widely employed in medical diagnoses [1,2], biomagnetic measurements [3,4], and fundamental physics [5,6]. Atomic magnetometers operating in the spin-exchange relaxation-free (SERF) regime have the advantages of high sensitivity and non-cryogenic operation [7], which play a significant role in magnetoencephalography (MEG) and magnetocardiography (MCG) [8–10].

However, traditional SERF atomic magnetometers can only detect one component of the magnetic fields. Nonetheless, multi-axis measurements can be realized by applying modulation technology or using a new configuration [11–15]. Li et al. realized a dual-axis magnetic measurement based on a pump–probe configuration in which a modulation field is applied along the direction of the pump light [16]. Seltzer and Romails described a three-axis SERF magnetometer by applying two low-frequency modulation fields [17]. The three components of the magnetic field were obtained from the DC and demodulated outputs. Osborne et al. demonstrated a dual-axis atomic magnetometer using only one pump beam and one rotating modulation field [18]. Xiao et al. reported a compact three-axis atomic magnetometer that uses only one pump beam [19]. The pump beam was reflected at 90° in the vapor cell, and the incident and reflected lights could detect the three components of the magnetic fields with three modulation magnetic fields. Boto et al. described a dual-pump light configuration with three modulation magnetic fields for triaxial measurements [20]. However, owing to numerous factors such as the non-orthogonality between the lights and coils, residual magnetic fields, and the light shift effect, these multi-axis atomic magnetometers are affected by the crosstalk effect, which can decrease the measurement accuracy.

Therefore, many researchers have studied the crosstalk effects in atomic magnetometers. Pradhan and Behera investigated this effect in a three-axis atomic magnetometer operated in the presence of a static magnetic field [21]. The three-axis response signal and the coupling response were measured and compared for static fields with different amplitudes. Li et al. analyzed the cross-axis isolation for a dual-axis atomic magnetometer based on longitudinal field modulation [22]. An analytical solution of the Bloch equation was obtained to optimize the modulation parameters and suppress the crosstalk effect. However, the simulation results were not verified experimentally. Furthermore, some researchers have only reported the value of the coupling coefficient for multi-axis atomic magnetometers [23,24] without a thorough investigation of the suppression and correction of the crosstalk effect.

We investigated this effect using a three-axis SERF atomic magnetometer and proposed an effective method to suppress it. First, we analyzed the influencing factors for this effect. Based on this, the modulation amplitude and frequency were optimized to improve the scale factors and reduce the coupling coefficient. Furthermore, a correction matrix, obtained by determining the inverse of the transfer matrix, was used to correct the output of the atomic magnetometer. In addition, the root mean square of the coupling coefficients was introduced to evaluate the correction performance. After the correction procedure, low coupling coefficients were obtained within the bandwidth of the three-axis atomic magnetometer. The proposed suppression method for the crosstalk effect can help improve the measurement accuracy and further promote the practical applications of the given magnetometer.

## 2. Methods

In the SERF regime, the time evolution of the alkali atomic spin is often described by the Bloch equation. The simpler Bloch equation can be derived from the density matrix equations (DMEs) when the spin-exchange rate is much faster than the precession frequency [7]. The spin-exchange relaxation rate should be considered for the Bloch equation, but the calculation methods are different and complicated for different types of magnetic fields [25]. Considering the three orthogonal modulation magnetic fields in this study, the accuracy of the spin-exchange relaxation rate calculation cannot be guaranteed. On the contrary, for calculations performed using the DMEs, only the spin-exchange rate  $R_{SE}$  is required. Therefore, the time evolution of the atomic spins for the three-axis atomic magnetometer in this study was described by the DMEs [26,27]:

$$\frac{d}{dt}\rho = \frac{1}{i\hbar}[H, \rho] + R_{SE}[\varphi(1 + 4\langle \mathbf{S} \rangle \cdot \mathbf{S}) - \rho] + R_{rel}[\varphi - \rho] + R_{op}[\varphi(1 + 2\mathbf{s} \cdot \mathbf{S}) - \rho] \quad (1)$$

where  $\rho$  is the density matrix,  $H = \gamma \mathbf{B} \cdot \mathbf{S}$  is the Hamiltonian,  $\gamma$  is the electronic gyromagnetic ratio,  $\mathbf{S}$  is the spin polarization vector,  $\langle \mathbf{S} \rangle$  is its expectation value,  $\mathbf{s}$  is the average photon spin,  $\varphi$  is the density matrix of the purely nuclear forces,  $R_{SE}$  is the spin-exchange rate,  $R_{op}$  is the optical pump rate, and  $R_{rel} = R_{SD} + R_{wall}$  is the spin-relaxation rate including the spin-destruction-relaxation rate  $R_{SD}$  and spin-relaxation rate  $R_{wall}$  due to wall collisions. The first term on the right-hand side of Equation (1) is the evolution due to Zeeman interactions. The second term describes the spin-exchange collisions between atoms. Finally, the third and fourth terms on the right-hand side represent the relaxation and optical pumping processes, respectively.

In this study, we investigated a three-axis magnetometer with two orthogonal pump lights, as shown in Figure 1 [20,28], which is a common configuration for three-axis measurements. Three modulation magnetic fields  $B_{mx} \sin(\omega_x \cdot t)\hat{x} + B_{my} \cos(\omega_y \cdot t)\hat{y} + B_{mz} \sin(\omega_z \cdot t)\hat{z}$  were simultaneously applied along the three orthogonal axes. The pump light along the  $x$ -axis was sensitive to the magnetic field along the  $y$ - and  $z$ -axes, while the light along the  $z$ -axis could measure the magnetic fields along the  $x$ - and  $y$ -axes. The three components of the magnetic field were measured by demodulating the two output signals.

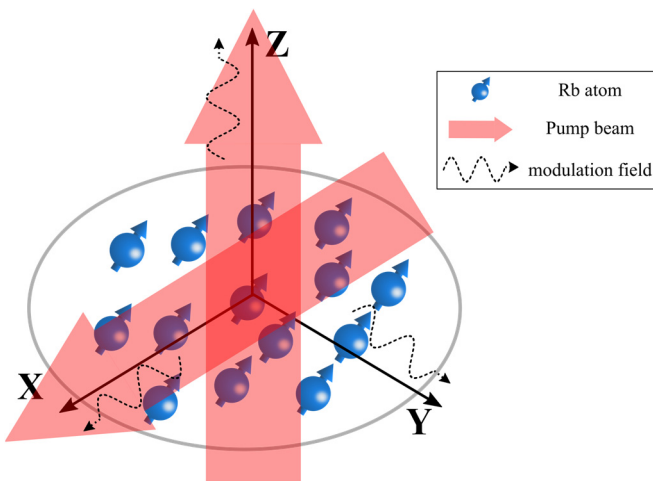


**Figure 1.** Diagram of three-axis magnetic field measurement. Two pump beams along  $x$ - and  $z$ -axes are used to polarize the alkali-metal atom.

As shown in Figure 2,  $B_x$ ,  $B_y$ , and  $B_z$  are the small magnetic fields along the  $x$ -,  $y$ -, and  $z$ -axes, respectively. The output of the atomic magnetometer was demodulated using different reference signals to obtain the demodulated response signals  $R_x$ ,  $R_y$ , and  $R_z$ .  $C_{11}$ ,  $C_{22}$ , and  $C_{33}$  were defined as the scale factors, while the others ( $C_{12}$ ,  $C_{13}$ ,  $C_{21}$ ,  $C_{23}$ ,  $C_{31}$ , and  $C_{32}$ ) were defined as the coupling factors.

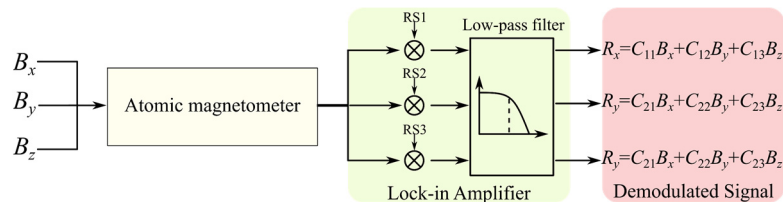


**Figure 2.** Schematic of the three-axis atomic magnetometer.  $R_x$ ,  $R_y$ , and  $R_z$  are the response signals and  $B_x$ ,  $B_y$ , and  $B_z$  are the magnetic fields to be measured. RS1, RS2, and RS3 are the reference signal with a frequency of  $\omega_x$ ,  $\omega_y$ , and  $\omega_z$ , respectively.

Under ideal conditions, the  $x$ -channel response signal  $R_x$  does not respond to  $B_y$  or  $B_z$  (i.e.,  $C_{12} = 0$  and  $C_{13} = 0$ ). However, a crosstalk effect generally exists in practice due to multiple reasons. For instance, in an integrated atomic magnetometer, installation error is inevitable when assembling the optical lens and coils. Therefore, there is a non-orthogonal angle between the lasers and magnetic coils [29], which can contribute to the crosstalk effect. Furthermore, the phase drift and error in the modulation and demodulation processes lead to demodulated signal leakage to other channels.

We quantified the crosstalk effect by defining the coupling coefficients in the  $x$ -channel [22]:

$$CT_{yx} = C_{12}/C_{11} \quad (2)$$

$$CT_{zx} = C_{13}/C_{11} \quad (3)$$

where  $CT_{yx}$  represents the error output in the  $x$ -channel owing to the magnetic field  $B_y$ , and  $CT_{zx}$  represents the error output in the  $x$ -channel owing to the magnetic field  $B_z$ . Similarly, we can define the coupling coefficients  $CT_{xy}$ ,  $CT_{zy}$ ,  $CT_{xz}$ , and  $CT_{yz}$  to describe the crosstalk effect in the  $y$ - and  $z$ -channels.

The relationship between the magnetic field vector  $\mathbf{B} = [B_x \ B_y \ B_z]^T$  and the demodulated output signal vector  $\mathbf{R} = [R_x \ R_y \ R_z]^T$  can be described as

$$\mathbf{R} = \mathbf{CB} \quad (4)$$

where  $\mathbf{C}$  is a  $3 \times 3$  transfer matrix,

$$\mathbf{C} = \begin{bmatrix} C_{11} & C_{12} & C_{13} \\ C_{21} & C_{22} & C_{23} \\ C_{31} & C_{32} & C_{33} \end{bmatrix} \quad (5)$$

From Equations (2) and (3), we find that the coupling coefficients are influenced by scale factors (diagonal elements of the transfer matrix  $\mathbf{C}$ ) and coupling factors (non-diagonal elements of the transfer matrix  $\mathbf{C}$ ). Therefore, we investigated the relationship between the scale factors and modulation parameters, including the modulation amplitude and frequency, by numerical simulation of the DMEs. Based on the simulation results, the modulation amplitude and frequency could be tuned to maximize the scale factors. Therefore, the crosstalk effect can be preliminarily reduced by optimizing the modulation parameters.

To further suppress the crosstalk effect, we proposed a signal processing method in which the inverse matrix of the transfer matrix  $\mathbf{C}$  was used to correct the demodulated output vector  $\mathbf{R}$ . Similar correction methods have been employed in triaxial fluxgate magnetometers [30,31]. As the SERF atomic magnetometer has a relatively narrow bandwidth (generally lower than 200 Hz in the open-loop mode) [18,32], the influence of the frequency response on the correction method should be considered.

A correction process was performed in the frequency domain to accurately determine the amplitude of the response signal. The demodulated output vector  $\mathbf{R}$  was converted into the frequency domain using a fast Fourier transform (FFT). A correction matrix  $\mathbf{P}$  was applied to correct the output signal  $\mathbf{R}$ :

$$\mathbf{R}_{\text{cor}}(f) = \mathbf{P}\mathbf{R}(f) \quad (6)$$

where  $\mathbf{P}$  is the correction matrix, and  $\mathbf{R}(f)$  and  $\mathbf{R}_{\text{cor}}(f)$  are the demodulated output signal vectors related to the signal frequency  $f$  before and after correction, respectively.

As the transfer matrices  $\mathbf{R}(f)$  are not the same at different frequencies, the corresponding correction matrices are also different. In this study, several groups of transfer matrices were measured at different frequencies within the bandwidth, and corresponding correction matrices were calculated. Each correction matrix was used to correct the demodulated output vectors. The root mean square of the coupling coefficients was introduced to evaluate the correction performance quantitatively.

$$CT_{rms} = \sqrt{\frac{1}{N} \sum_{n=1}^N [CT_{xy}^2(f_n) + CT_{yx}^2(f_n) + CT_{xz}^2(f_n) + CT_{zx}^2(f_n) + CT_{yz}^2(f_n) + CT_{zy}^2(f_n)]} \quad (7)$$

where  $f_n$  is the signal frequency;  $CT_{xy}(f_n)$ ,  $CT_{yx}(f_n)$ ,  $CT_{xz}(f_n)$ ,  $CT_{zx}(f_n)$ ,  $CT_{yz}(f_n)$ , and  $CT_{zy}(f_n)$  are the coupling coefficients after the correction process; and  $N$  is the number of data groups.

### 3. Experimental Setup and Procedure

The experimental setup is illustrated in Figure 3. A cubic glass cell with an inner length of 8 mm was filled with a drop of  $^{87}\text{Rb}$ , 2100 Torr  $^4\text{He}$  as the buffer gas, and 70 Torr  $\text{N}_2$  as the quenching gas, which was heated to 423 K using two flexible heating films. To avoid magnetic interference from the heater current, the heating films were designed to suppress the magnetic field using a genetic algorithm [33] and were driven by a current with a frequency of 500 kHz [34]. The cell temperature was monitored using a non-magnetic sensor Pt1000 and controlled using a PID program.

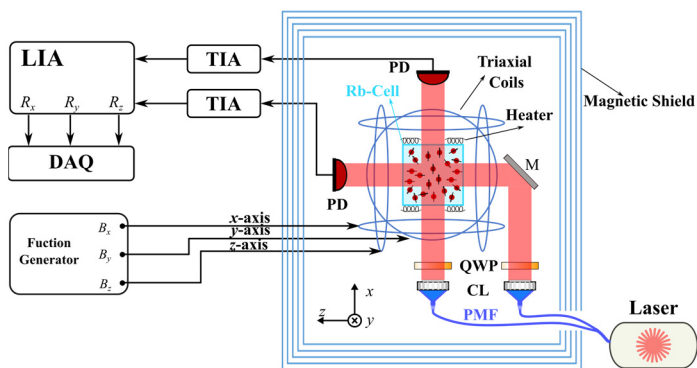


**Figure 3.** The setup of the dual-axis atomic magnetometer. PMF: polarization-maintaining fiber; CL: collimating lens; QWP: quarter-wave plate; PD: photodiode; TIA: trans-impedance amplifier; LIA: lock-in amplifier; DAQ: data acquisition equipment.

An external cavity laser (Toptica DL Pro) provided two pump lights that were introduced into the atomic magnetometer using polarization-maintaining fibers. The optical power density of each pump beam was set to  $12 \text{ mW/cm}^2$ , and the laser wavelength was 794.96 nm. The laser beam was converted into circularly polarized light using a quarter-wave plate. The pump light from the cell was collected by a photodiode. The photocurrent generated from the photodiode was transferred to a voltage signal using a trans-impedance amplifier, which was then demodulated by a lock-in amplifier (Zurich Instruments, MFLI). The demodulated signals,  $R_x$ ,  $R_y$ , and  $R_z$  were acquired using data acquisition equipment for analysis and processing.

A four-layer cylindrical  $\mu$ -metal magnetic shield was employed to provide a near-zero magnetic field to the atomic magnetometer. A triaxial coil was mounted around the vapor cell, which was driven by a function generator (Keysight 33522 B). The coils were applied to nullify the residual magnetic field in the magnetic shield [35] and generate the modulation magnetic fields to manipulate the alkali metal atoms.

In the following sections, the scale factors (i.e., the diagonal elements of the transfer matrix) were increased by optimizing the modulation parameters (modulation amplitude and frequency). With an increase in the scale factors, the coupling coefficients were reduced according to Equations (2) and (3). The transfer matrices at different frequencies were experimentally calibrated. Finally, a correction matrix was employed to suppress the crosstalk effect.

#### 4. Result and Discussion

##### 4.1. Optimization of the Modulation Parameters

As mentioned in the Methods section, the three-channel scale factors were optimized to reduce the coupling coefficients. First, the relationship between the scale factors and the modulation amplitude was investigated by numerical simulation of the DMEs. The three-axis modulation frequency was set to 1 kHz. As shown in Figure 4, the simulation results (i.e., the orange curve) indicate that the scale factor increased with the modulation amplitude, reaching a maximum value at an amplitude of 13 nTrms. On the further increase in amplitude, the scale factor decreased. Employing the optimization value of the modulation amplitude, the relationship between the scale factors and modulation frequency was simulated using the DMEs. As shown in Figure 5, the simulation value of the scale factor (i.e., the orange curve) decreased with modulation frequency in the range of 0.8 kHz to 2.0 kHz. There was no maximum for the scale factors in the simulation range. It should be noted that the simulation results of  $C_{11}$ ,  $C_{22}$ , and  $C_{33}$  were the same, so only one simulation curve is plotted in Figures 4 and 5.

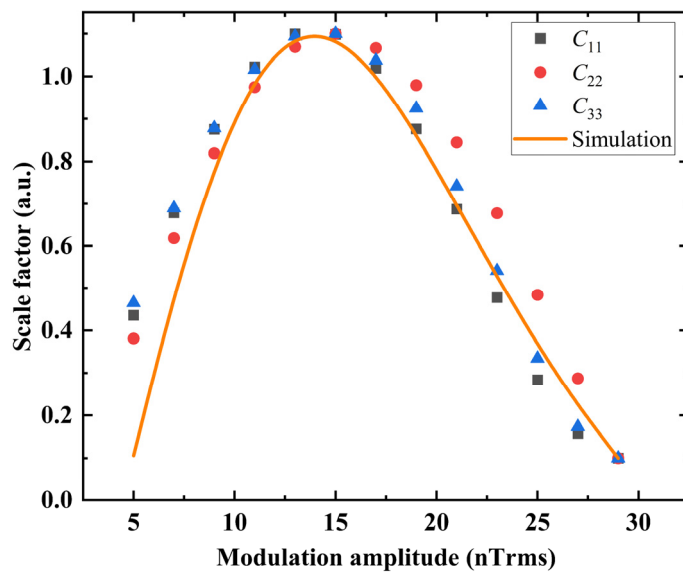


**Figure 4.** Three-channel scale factors under different modulation amplitudes. The square, round, and triangular points represent the experimental results. The orange curve is the simulation result.

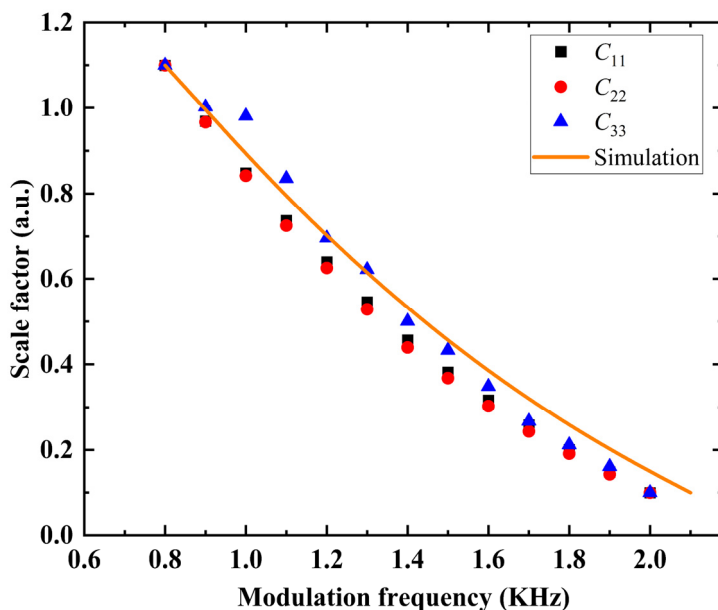


**Figure 5.** Three-axis scale factors under different modulation frequencies. The square, round, and triangular points represent the experimental results. The orange curve is the simulation result.

Based on the simulation results, the modulation amplitude and frequency were optimized experimentally. The three-channel scale factors  $C_{11}$ ,  $C_{22}$ , and  $C_{33}$  were investigated under different modulation parameters through experiments and simulations. An AC calibration field with an amplitude of 100 pTrms at 30.5 Hz was applied along the  $x$ -,  $y$ -, and  $z$ -axis. The scale factors for different modulation parameters were measured to verify the consistency between the experiment and the simulation. As shown in Figures 4 and 5, the changing trend of the three-channel scale factors was in good agreement with the simulation results. After the optimization, all the coupling coefficients were less than 6%.

#### 4.2. Correction of the Transition Matrix

The frequency responses in all the channels were measured by applying a sinusoidal magnetic field with an amplitude of 100 pTrms along the three axes in turn. As shown in

Figure 6, the response signals were slightly different among the three channels because of the non-orthogonality of the magnetic coil and lights. The frequency response was fitted using a first-order low-pass filter [36],

$$H(s) = \frac{G_0}{1 + s/\omega_c} \quad (8)$$

where  $\omega_c$  is the cutoff angular frequency, and  $G_0$  is the DC response factor.

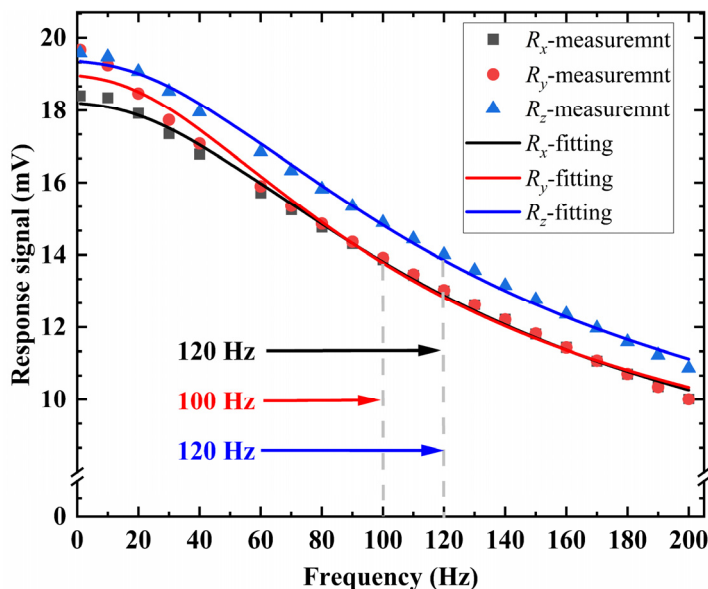


**Figure 6.** The three-channel frequency response signal and the fitting curves. The bandwidths were 120 Hz, 100 Hz, and 120 Hz in  $x$ -,  $y$ -, and  $z$ -channel, respectively.

According to the fitting results, the bandwidths were 120 Hz, 100 Hz, and 120 Hz in  $x$ -,  $y$ -, and  $z$ -channel, respectively.

The transfer matrices at different frequencies were calibrated within the atomic magnetometer bandwidth. Following the results in the previous section, the modulation frequency and amplitude were set to 1 kHz and 13 nTrms, respectively, to maximize the signal response. Ten calibration signals with amplitudes of 100 pTrms and different frequencies were applied along the three axes. The three-channel response signals were simultaneously collected by applying the calibration magnetic field along the  $x$ -,  $y$ -, and  $z$ -axis sequentially. The demodulated output was analyzed in the frequency domain using FFT. The coupling factors (i.e., the nondiagonal elements of the transfer vector) are shown in Figure 7. As the frequency of the magnetic field increased, the coupling scale factors decreased in every channel.

After calibrating the transfer matrix and coupling scale factors, the correction matrices at different frequencies were calculated. Each correction matrix was used to correct the demodulation output. The values of the root mean square of the three-channel coupling coefficients for these ten groups of data were calculated using Equation (7) and compared to obtain the most suitable correction matrix. The correction matrix at 40 Hz exhibited the best suppression performance for the crosstalk effect. Therefore, all the demodulated signals at different frequencies were corrected using this matrix, which was the inverse matrix of the transfer matrix at 40 Hz. As shown in Figure 8, the coupling coefficients before and after the correction were compared at different frequencies. The cold-color groups were the coupling coefficients before the correction, and the warm-color groups were the ones after the correction. Before the correction, the coupling coefficients diverged at different frequencies. The highest coupling coefficient was the  $CT_{zy}$  at 1 Hz, which was approximately 5.74%, and the lowest one was less than 1%. After the correction, all coupling coefficients were reduced to below 3%, with the majority being lower than 1%.

as shown in Figure 8. As the correction matrix was calculated from the transfer matrix at 40 Hz, the coupling coefficients at 40 Hz were approximately zero after correction.

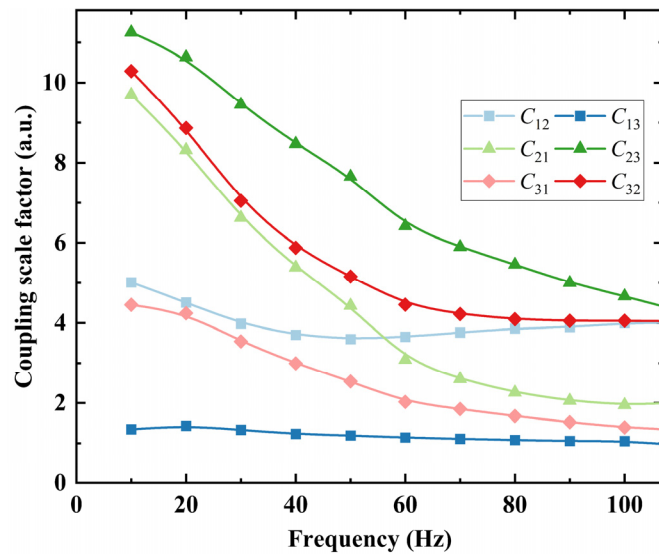


**Figure 7.** The coupling scale factors at different frequencies. The data was collected within the bandwidth of the atomic magnetometer.

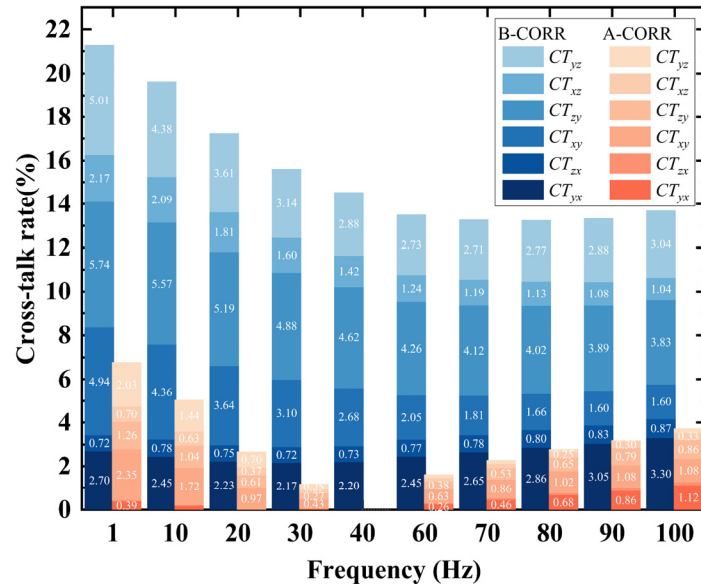


**Figure 8.** The coupling coefficient before and after correction. In the illustration, the left column represents the coupling coefficient before correction (B-CORR), and the right column is the data after correction (A-CORR). The correction matrix was the inverse matrix of the transfer matrix at 40 Hz. The values below 0.25% are not marked on the figure.

## 5. Conclusions

In this study, we investigated the crosstalk effect in a three-axis SERF atomic magnetometer. The optimization values of the modulation parameters were determined based on the simulation results. In the experiment, the value of the coupling coefficient was less than 6% using the simulation optimization parameters. To further suppress the crosstalk effect, a correction method was proposed. The inverse of the transfer matrix was used to correct the output signal. After the correction, all the coupling coefficients were reduced to less than 3%, most of which were lower than 1%. The investigation and suppression of the crosstalk effect in this study can help improve the practicality of the three-axis SERF atomic

magnetometer, which would further contribute to various applications such as medical diagnosis, fundamental physics, and biomagnetic measurement.

**Author Contributions:** Conceptualization, Y.Y. and B.Z.; methodology, Y.Y., J.L. and B.Z.; validation, Y.Y. and J.L.; formal analysis, Y.Y., K.W. and W.W.; investigation, Y.Y., K.W. and Z.L.; data curation, Y.Y., Z.L. and X.L.; writing—original draft preparation, Y.Y.; writing—review and editing, J.L. and B.Z.; supervision, B.Z. and G.L.; project administration, Y.Y. and J.L.; funding acquisition, J.L. All authors have read and agreed to the published version of the manuscript.

**Funding:** This work was supported by Key R&D Program of Zhejiang, China (No. 2020C01037) and the National Natural Science Foundation of China under Grant (No. 61903013).

**Institutional Review Board Statement:** Not applicable.

**Informed Consent Statement:** Not applicable.

**Data Availability Statement:** The data presented in this study are available on reasonable request from the corresponding author.

**Conflicts of Interest:** The authors declare no conflict of interest.

## References

- Burgess, R.C. MEG for Greater Sensitivity and More Precise Localization in Epilepsy. *Neuroimaging Clin. N. Am.* **2020**, *30*, 145–158. [[CrossRef](#)] [[PubMed](#)]
- Soheilian, A.; Tehranchi, M.M.; Ranjbaran, M. Detection of magnetic tracers with  $M_x$  atomic magnetometer for application to blood velocimetry. *Sci. Rep.* **2021**, *11*, 7156. [[CrossRef](#)] [[PubMed](#)]
- Rea, M.; Holmes, N.; Hill, R.M.; Boto, E.; Leggett, J.; Edwards, L.J.; Woolger, D.; Dawson, E.; Shah, V.; Osborne, J.; et al. Precision magnetic field modelling and control for wearable magnetoencephalography. *NeuroImage* **2021**, *241*, 118401. [[CrossRef](#)] [[PubMed](#)]
- Kim, Y.J.; Savukov, I.; Newman, S. Magnetocardiography with a 16-channel fiber-coupled single-cell Rb optically pumped magnetometer. *Appl. Phys. Lett.* **2019**, *114*, 143702. [[CrossRef](#)]
- Smiciklas, M.; Brown, J.M.; Cheuk, L.W.; Smullin, S.J.; Romalis, M.V. New Test of Local Lorentz Invariance Using a  $^{21}\text{Ne}$ -Rb-K Comagnetometer. *Phys. Rev. Lett.* **2011**, *107*, 171604. [[CrossRef](#)]
- Padniuk, M.; Kopciuch, M.; Cipolletti, R.; Wickenbrock, A.; Budker, D.; Pustelny, S. Response of atomic spin-based sensors to magnetic and nonmagnetic perturbations. *Sci. Rep.* **2022**, *12*, 324. [[CrossRef](#)]
- Ledbetter, M.P.; Savukov, I.M.; Acosta, V.M.; Budker, D.; Romalis, M.V. Spin-exchange-relaxation-free magnetometry with Cs vapor. *Phys. Rev. A* **2008**, *77*, 033408. [[CrossRef](#)]
- Yang, Y.; Xu, M.; Liang, A.; Yin, Y.; Ma, X.; Gao, Y.; Ning, X. A new wearable multichannel magnetocardiogram system with a SERF atomic magnetometer array. *Sci. Rep.* **2021**, *11*, 5564. [[CrossRef](#)]
- Clancy, R.J.; Gerginov, V.; Alem, O.; Becker, S.; Knappe, S. A study of scalar optically-pumped magnetometers for use in magnetoencephalography without shielding. *Phys. Med. Biol.* **2021**, *66*, 175030. [[CrossRef](#)]
- Marhl, U.; Sander, T.; Jazbinšek, V. Simulation Study of Different OPM-MEG Measurement Components. *Sensors* **2022**, *22*, 3184. [[CrossRef](#)]
- Huang, H.; Dong, H.; Chen, L.; Gao, Y. Single-beam three-axis atomic magnetometer. *Appl. Phys. Lett.* **2016**, *109*, 062404. [[CrossRef](#)]
- Zheng, W.; Su, S.; Zhang, G.; Bi, X.; Lin, Q. Vector magnetocardiography measurement with a compact elliptically polarized laser-pumped magnetometer. *Biomed. Opt. Express* **2020**, *11*, 649–659. [[CrossRef](#)] [[PubMed](#)]
- Zhivun, E.; Bulatowicz, M.; Hryciuk, A.; Walker, T. Dual-axis pi-pulse spin-exchange relaxation-free magnetometer. *Phys. Rev. Appl.* **2019**, *11*, 034040. [[CrossRef](#)] [[PubMed](#)]
- Namita, K.; Ito, Y.; Kobayashi, T. Vector measurement of pico tesla magnetic fields using an optically pumped magnetometer by varying pump beam direction. *Jpn. J. Appl. Phys.* **2021**, *60*, 076507. [[CrossRef](#)]
- Lu, F.; Lu, J.; Li, B.; Yan, Y.; Zhang, S.; Yin, K.; Ye, M.; Han, B. Triaxial Vector Operation in Near-zero Field of Atomic Magnetometer with Femtotesla Sensitivity. *Trans. Instrum. Meas.* **2022**, *71*, 1501210. [[CrossRef](#)]
- Li, Z.; Wakai, R.T.; Walker, T.G. Parametric modulation of an atomic magnetometer. *Appl. Phys. Lett.* **2006**, *89*, 134105. [[CrossRef](#)]
- Seltzer, S.J.; Romalis, M.V. Unshielded three-axis vector operation of a spin-exchange-relaxation-free atomic magnetometer. *Appl. Phys. Lett.* **2004**, *85*, 4804–4806. [[CrossRef](#)]
- Osborne, J.; Orton, J.; Alem, O.; Shah, V. Fully integrated, standalone zero field optically pumped magnetometer for biomagnetism. In Proceedings of the Steep Dispersion Engineering and Opto-Atomic Precision Metrology XI, San Francisco, CA, USA, 27 January–1 February 2018; Volume 10548, p. 105481G. [[CrossRef](#)]
- Xiao, W.; Wu, Y.; Zhang, X.; Feng, Y.; Sun, C.; Wu, T.; Chen, J.; Peng, X.; Guo, H. Single-beam three-axis optically pumped magnetometers with sub-100 femtotesla sensitivity. *Appl. Phys. Express* **2021**, *14*, 066002. [[CrossRef](#)]

20. Boto, E.; Shah, V.; Hill, R.M.; Rhodes, N.; Osborne, J.; Doyle, C.; Holmes, N.; Rea, M.; Leggett, J.; Bowtell, R.; et al. Triaxial detection of the neuromagnetic field using optically-pumped magnetometry: Feasibility and application in children. *NeuroImage* **2022**, *252*, 119027. [[CrossRef](#)]
21. Pradhan, S.; Behera, R. Characterization of polarimetric based three axis atomic magnetometer. *Sens. Actuators A Phys.* **2019**, *290*, 48–53. [[CrossRef](#)]
22. Li, Y.; Ma, M.; Luo, Y.; Xie, Y.; Wang, J.; Xu, F. Discussion of cross-axis isolation in vector atomic magnetometry via longitudinal field modulation. In Proceedings of the 2021 International Conference of Optical Imaging and Measurement (ICOIM), Xi'an, China, 27–29 August 2021; pp. 234–238. [[CrossRef](#)]
23. Tang, J.; Zhai, Y.; Zhou, B.; Han, B.; Liu, G. Dual-Axis Closed Loop of a Single-Beam Atomic Magnetometer: Toward High Bandwidth and High Sensitivity. *IEEE Trans. Instrum. Meas.* **2021**, *70*, 1504808. [[CrossRef](#)]
24. Huang, H.C.; Dong, H.F.; Hu, X.Y.; Chen, L.; Gao, Y. Three-axis atomic magnetometer based on spin precession modulation. *Appl. Phys. Lett.* **2015**, *107*, 182403. [[CrossRef](#)]
25. Xiao, W.; Wu, T.; Peng, X.; Guo, H. Atomic spin-exchange collisions in magnetic fields. *Phys. Rev. A* **2021**, *103*, 043116. [[CrossRef](#)]
26. Happer, W.; Tam, A.C. Effect of rapid spin exchange on the magnetic-resonance spectrum of alkali vapors. *Phys. Rev. A* **1977**, *16*, 1877–1891. [[CrossRef](#)]
27. Savukov, I.M.; Romalis, M.V. Effects of spin-exchange collisions in a high-density alkali-metal vapor in low magnetic fields. *Phys. Rev. A* **2005**, *71*, 023405. [[CrossRef](#)]
28. Yan, Y.; Yan, Y.; Lu, J.; Lu, J.; Zhang, S.; Zhang, S.; Lu, F.; Lu, F.; Yin, K.; Yin, K.; et al. Three-axis closed-loop optically pumped magnetometer operated in the SERF regime. *Opt. Express* **2022**, *30*, 18300–18309. [[CrossRef](#)]
29. Li, S.; Lu, J.; Ma, D.; Wang, K.; Gao, Y.; Sun, C.; Han, B. In Situ Measurement of Nonorthogonal Angles of a Three-Axis Vector Optically Pumped Magnetometer. *IEEE Trans. Instrum. Meas.* **2022**, *71*, 7001109. [[CrossRef](#)]
30. Goleman, K.; Sasada, I. A Triaxial Orthogonal Fluxgate Magnetometer Made of a Single Magnetic Wire With Three U-Shaped Branches. *IEEE Trans. Magn.* **2007**, *43*, 2379–2381. [[CrossRef](#)]
31. Shi, J. Adaptive calibration algorithm of three axial magnetic fluxgate sensor using support vector regression. In Proceedings of the 2010 Chinese Control and Decision Conference, Xuzhou, China, 26–28 May 2010; pp. 4222–4225. [[CrossRef](#)]
32. Shah, V.K.; Wakai, R.T. A compact, high performance atomic magnetometer for biomedical applications. *Phys. Med. Biol.* **2013**, *58*, 8153–8161. [[CrossRef](#)]
33. Lu, J.; Lu, C.; Wang, S.; Zhang, X.; Zhang, S.; Lu, F. Optimized electric heater configuration design with magnetic-field self-suppression using genetic algorithm. *Sens. Actuators A Phys.* **2022**, *344*, 113758. [[CrossRef](#)]
34. Lu, J.; Qian, Z.; Fang, J.; Quan, W. Effects of AC magnetic field on spin-exchange relaxation of atomic magnetometer. *Appl. Phys. B* **2016**, *122*, 59. [[CrossRef](#)]
35. Zhang, S.; Zhang, S.; Zhang, K.; Zhang, K.; Zhou, Y.; Ye, M.; Ye, M.; Lu, J.; Lu, J.; Lu, J.; et al. Triaxial precise magnetic field compensation of a zero-field optically pumped magnetometer based on a single-beam configuration. *Opt. Express* **2022**, *30*, 24579–24588. [[CrossRef](#)]
36. Allred, J.C.; Lyman, R.N.; Kornack, T.W.; Romalis, M.V. High-Sensitivity Atomic Magnetometer Unaffected by Spin-Exchange Relaxation. *Phys. Rev. Lett.* **2002**, *89*, 130801. [[CrossRef](#)] [[PubMed](#)]